A new damage detection technique based on wave propagation for rails

G. Zumpano, M. Meo [*]

Crashworthiness, Impact and Structural Mechanics Group, SoE, Cranfield University, Bedford, MK 43 0AL, UK

Abstract

This paper presents a novel damage detection technique, tailored at the identification of structural surface damage on rail structures. The damage detection, proposed in this paper, exploits the wave propagation phenomena (P, S, Rayleigh and guided wave velocities) by identifying discrepancies, due to damage presence, in the dynamic behaviour of the structure. The uncorrelations are generated by waves reflected back to the sensor locations by the flaw surfaces. The peculiarity of the presented approach is the use of a time frequency coherence function for the identification of the arrivals of guided wave reflected back to the sensors by the damage surfaces.

The damage detection methodology developed was divided into three steps. In the first step, the presence of the damage on the structure was assessed. In the second step, the arrival time of the reflected wave (or echo) was estimated using the continuous wavelet transform. Then, the detection algorithm was able, through a ray-tracing algorithm, to estimate the location of damage.

A numerical investigation of two single damages was carried out. The damage was introduced on the railhead surface to simulate rolling contact fatigue defects. The results showed that the proposed methodology can be used successfully to localise the damage location, however, as expected, the localisation is strongly affected by the frequency range used. The results suggested that the separation and the characterisation of single modes are crucial for the identification of different types of rail defects. Further work is needed to establish the damage severity by relating the magnitude of the changes of the time frequency coherence to reflection and attenuation coefficients of each guided wave used and on the selection of the best range of frequency according to the type of damage to be identified.
© 2005 Elsevier Ltd. All rights reserved.

Keywords: Rails; Damage detection; Wave propagation; Wavelets; Ray tracing

[*] Corresponding author. Tel. +44 1234 750111x5220; fax +44 1234 752149.
    E-mail address: m.meo@cranfield.ac.uk (M. Meo).

1. Introduction

Since the earliest days of railroading, maintenance was a main concern. Nowadays, maintenance issues are becoming overwhelming because of the increase of operating loads, traffic, and high-speed trains. Therefore, today, maintenance means prevention of catastrophic rail failure to avert loss of rolling material as well as of lives. The figures involved are staggering, only in the EU the cost related to rail failures is around €2 billion per year (Cannon et al., 2003). The number of derailments in the United States on 2001 was 290 according to Federal Railroad Administration for a total cost of €97 million (Cannon et al., 2003). However, these estimates are only approximations of the real data, since national railways are reluctant to ascribe specific causes to accidents. Nonetheless, the stakes are so huge that the International Union of Railways (UIC) made of the rail defect management (RDM), its fist World Joint Research Project (Lundgren et al., 2001). RDM is the process that controls the formation and the propagation of defects on the rails through regular inspections and the implementation of prescribed actions when these are found.

Rail defects have been classified in many ways. In this paper, rail defects were classified based on their origins (Cannon et al., 2003). There are three broad families of defects: rail manufacturing defects, improper use or handling rail defects, and rail wear and fatigue.

Rail manufacturing defects are generally inclusions of non-metallic origin or wrong local mixings of the rail steel components that, under operative loads, generate local concentration of stresses, which trigger the rail failure process (Murav'ev and Boyarkin, 2003). A convenient classification of this class of rail defects is based on the direction of propagation of the flaws under operative loads. Two types of damages are classified (Abbaszadeh et al., 2003; Jeffrey and Peterson, 1999):

- *Transverse defects*: any progressive fracture that occurs in the head of rails with a transverse direction. This type of defect account for the 29% of train derailments in the USA between 1992 and 1995 (Jeffrey and Peterson, 1999) (the total number of derailments in this periods was 554 for a cost of $70 million).
- *Longitudinal defects*: any internal progressive fracture that propagates longitudinally in the rails. There are two longitudinal defects, the vertical split heads, and the horizontal split head. According to the Federal Railroad Administration this type of damage is the cause of the 43% of derailments between the 1992 and 1995 (Jeffrey and Peterson, 1999).

Defects deriving from improper use or handling of rails are generally due to spinning of train wheels on rails or sudden train brakes. An example of this type of damage is the wheelburn defect. The last class of defects is due to wearing mechanisms of the rolling surface and/or to fatigue. In this flaw typology, three defects are the most frequent: corrugation, rolling contact fatigue (RCF) damage and bolt-hole cracks. Corrugation is an event strictly correlated to the wearing of the railhead, generated by a wavelength-fixing mechanism related to train speed, distance between the sleepers (Vadillo et al., 1998), friction (Eadie et al., 2000) and so on. Six type of corrugation can be identified (Mueller, 2000): heavy haul corrugation, light rail corrugation, corrugation on resiliently booted sleepers, contact fatigue corrugation in curves, rutting and roaring rails or short-pitch corrugation.

The corrugation itself does not compromise rolling safety, but has an adverse effect on track elements and rolling stocks by increasing noise emissions, loading and fatigue (Bohmer and Klimpel, 2002).

RCF damages are much more severe from the point of view of the structure integrity (Cannon et al., 2003; Cannon and Pradier, 1996; Grassie et al., 2002). The fatigue crack initiates on or very close to the rail rolling surface, which is not related to any material defect (Cannon and Pradier, 1996). Its occurrence is increasing on high speed passenger lines, mixed and heavy haul railways and can lead to expensive rail grinding in the attempt to remove it, premature removal of the rails and complete rail failure.

The rolling contact fatigue damage on rails can be divided in headchecks, squats and spalling. RCF damages incidence can be reduced by lubricating rolling surfaces. Although, fluid entrapment in the metal is one of the most common causes for speeding up the surface initiated crack growth (Cannon et al., 2003).

Bolt-hole cracks account for about the 50% of the rail defects in joined tracks (Jeong, 2001). These cracks originate on the closest bolt-hole surface to the rail end and propagate with an angle ±45° from the vertical until the web-railhead junction. Fretting fatigue of the bolt shank against the hole surface is believed to be the principal cause of this typology of crack.

2. Overview of current inspection techniques

The first type of inspection ever used was the visual inspection. A sands mirror inspector was capable of inspecting one mile of rail per day. Unfortunately, many external and internal defects are overlooked in this way. Since 1923 with the invention of the rail flaw detector car, based on the induction method developed by Herring in 1877, inspection cars have been the most common way to inspect railroads (Abbaszadeh et al., 2003). In the 1960s the induction detector was integrated with ultrasonic sensors, since then, this has been the standard for inspection cars (Clark, 2004). The induction technique exploits electromagnetic phenomena. Basically, the rail becomes part of a circuit, where an ampere generator through brushes, in contact with the rail surface, injects high currents, which in presence of a defect are distorted. This distortion of the current flux in the rails generates discrepancies, in the associated magnetic field, detected by a special designed group of sensors placed on the inspection car (Clark, 2004). Recently, a non-contact induction technique based on eddy currents was developed (Oukhellou et al., 1999). This method does not employ brushes to close the circuit with the rail, but uses, instead, a magnetic core to induce eddy currents in the rail, which losses are correlated to the damage presence. However, although this technology allows using bogies of a standard railway car or coach at the standard speed of the line, only damages on the surface, or close to it, can be monitored. This is a common problem of induction techniques, which are not capable of penetrating in depth the railhead. This is the reason why, as mentioned previously, in the 1960s ultrasonic inspection (Cannon et al., 2003; Jeffrey and Peterson, 1999; Jeong, 2001; Clark, 2004; Oukhellou et al., 1999; Marais and Mistry, 2003; Markov et al., 2003) was introduced and used together with or in alternative at the induction inspection. Ultrasonic techniques scan railhead through ultrasonic beams and detect the return of reflected or scattered energy using ultrasonic transducers. The amplitude of the reflections and their arrival times indicate the presence, the location and the severity of the damage (Clark, 2004). Although, ultrasonic testing is capable of inspecting the whole railhead (Marais and Mistry, 2003), it has several drawbacks such as:

- *Limited ultrasonic inspection car speeds (*Cannon et al., 2003*).* These are generally much slower than the line speed compelling the inspection operation to be carried out outside the commercial track periods, in order to avoid disruption at the normal train timetables. Typical operational speeds are between 40 and 70 km/h, although, a new generation of ultrasonic devices can work up to 100 km/h. Unfortunately, these speeds are theoretical, because if a damage is detected the inspection crew, generally, checks immediately the nature and the severity of the damage, reducing the inspection speed to an average of 15 km/h.
- *Shallow crack shadowing (*Cannon et al., 2003*; Jeffrey and Peterson, 1999).* Small shallow cracks can shadow much more severe cracks by reflecting the ultrasonic beams, preventing so the detection of deeper defects (Fig. 1).
- *False defect detection.* Current data reports that from 70% to 80% of the defect detection reveals to be false during the hand test verification. This contributes to a further slowing down of the inspection operations.

Fig. 1. Shallow crack shadowing.

In the last decade other inspection techniques were developed and investigated for rail inspection application. Some of them are reported below:

- *A photothermal method (*Mandelis et al., 1999*)*. This consists in a laser beam modulated at certain frequencies that hits the surface under study and being diffused in thermal-waves, which are captured by a thermal detector. Because of the heavy dumped nature of the thermal-waves, this technique is suitable only for detecting superficial flaws.
- Corrugation detection techniques based on either image processing through Gabor filtering (Mandriota et al., 2001) or Barkhaunes-noise correlation (Takacs et al., 2002).
- *Elastic guided waves propagating through the rail*. The technique exploits the capability of some guided wave modes to travel great distance, e.g. 2000 m, allowing also the possibility to check for the damage throughout the rail cross-section (Rose et al., 2004; Rose, 2000). Other guided wave based damage detection techniques on rails exploits reflection coefficient spectra (Lanza di Scalea and McNamara, 2003) and wave mode conversion signatures for various defects (Cawley et al., 2002; Wilcox et al., 2003).
- *Air coupled ultrasonic test methods*. These techniques used non-contact ultrasonic sensors to monitor rails by analysing resonant standing waves (Lanza di Scalea and McNamara, 2003) and signal energy loss (Kenderian et al., 2001).
- *Acoustic emission (AE)*. The technique has been applied on a scaled test rig. The results did not show the hoped AE activity of the surface damages, although, changes in the vibration activity of the test rig due to seeded surface damages were recorded (Bruzelius and Mba, 2004).

3. Damage detection methodology

While convectional ultrasonic inspection (Rose et al., 2004; Rose, 2000) uses ultrasonic beams propagating through the structure thickness, the proposed damage detection approach (wave propagation based damage detection (WPBDD) algorithm) exploits the wave propagation phenomena (P, S, Rayleigh and guided waves) (Graff, 1975) by identifying the discrepancies, due to damage presence, in the dynamic behaviour of the structure using a time–frequency coherence function. The purpose of this function is to identify any possible uncorrelation (discrepancy) present between two time histories. The first time history is used as reference and must be acquired when the structure is in pristine conditions, while the second time signal is used to monitoring the health state of the rails, and it can be acquired every time a trigger condition is satisfied. Physically, the discrepancies are generated by waves (P, S, Rayleigh and guided waves) reflected back to the sensor locations by the flaw surfaces, which in its absence would not exist. Because the coherence function is defined in the time–frequency space, the arrivals of the perturbation waves, generated by the damage presence, are identified in terms of their arrival times, which is a function of the frequency. By calculating the arrival time of the waves interacting with the defect surfaces, the detection algorithm is able, through a ray-tracing algorithm, to estimate the damage location. Differently from similar techniques, the main advantages of the proposed methodology is that there is no need to control the excitation force

nor an expert ultrasonic testing inspector to discriminate between boundary and damage reflected waves (Rose et al., 2004; Rose, 2000; Franklin et al., 2001; Viktorov, 1967; Hay and Rose, 2002; Cawley et al., 2002). Moreover, since a vibration wave can propagate within a medium on large distances with a very little amplitude loss, a single sensor can inspect large portion of the structures in few instants, in contrast with conventional ultrasonic techniques, where a number of very expensive scans are needed to inspect the same area.

4. Continuous wavelet transform

The central piece of the methodology here presented is the time–frequency coherence function. The main reason of working in the time frequency space lays in the drawbacks of the standard ultrasonic techniques developed in either the time or the frequency domain (Angrisani and Daponte, 1997), since their performances decrease consistently in presence of echo overlap, attenuation phenomena at high frequencies and critical sampling. Those limitations can be overcome by the introduction of time frequency representations (TFRs) (Angrisani and Daponte, 1997), which adoption increases the accuracy of the measures, reduces the attenuation phenomena and allows careful control between overlapped echoes.

A comparison performed between the two most common TFRs (Angrisani and Daponte, 1997), the short time Fourier transformation (STFT) and the continuous wavelet transformation (CWT), showed that the CWT is better in terms of time resolution offered at high frequency and in terms of noise withstanding. For this reasons, the CWT was used as TFRs for the damage detection technique developed.

Wavelets are the natural evolution of the STFT (Chen and Ling, 2002; Mallat, 1998). They linearly decompose an arbitrary signal $s(t)$ by projecting it on functions that are simply dilations and translations of a parent (or mother) wavelet $g(t)$ via the convolution of the signal and the scaled/shifted parent wavelet (Teolis, 1998; Kareem and Kijewski, 2002)

$$\mathrm{CWT}(a,t) = \frac{1}{\sqrt{a}} \int_{-\infty}^{\infty} s(\tau) g^* \left(\frac{t-\tau}{a} \right) \mathrm{d}\tau \tag{1}$$

where a is the dilation parameter and τ is the translation parameter.

The selection of the mother wavelet to employ is not an easy task, because the number of parent wavelets (or mother wavelet), present in literature, are countless and their application the most various. However, the most used is the complex Morlet wavelet (Kareem and Kijewski, 2002; Legendre et al., 2001; Gilliam et al., 2000; Staszwski, 1997), because of its particularity of giving, at the same time, magnitude and phase information, very useful to visualize possible discontinuities. Moreover, this wavelet becomes very attractive for harmonic analysis, due to its analogies with the Fourier transforms expressed by this equation (Teolis, 1998)

$$g(t) = \frac{1}{\sqrt{\pi\gamma}} \mathrm{e}^{-\frac{t^2}{\gamma}} (\cos(\omega_0 t) + \mathrm{i}\sin(\omega_0 t)) \tag{2}$$

Basically, Morlet wavelets are a Gaussian-windowed Fourier transform, with a central frequency $f_0 = \omega_0/2\pi$ and the width of the Gauss curve (the wavelet frequency band) γ. By maximising Eq. (2) in the frequency domain (Eq. (4)) (Teolis, 1998) a unique relation between the dilation parameter a and frequency f is obtained

$$f = \frac{a}{f_0} \tag{3}$$

$$G(af) = \mathrm{e}^{-\pi^2 \gamma (af - f_0)} \tag{4}$$

Hence, because of this unique relation the Morlet wavelet was chosen as parent wavelet.

5. Wave propagation based damage detection

The damage detection methodology developed was split in three steps. In the first step, the presence of the damage on the structure was assessed. In the second step, the arrival time of the reflected wave (or echo) was estimated, and in the third step the damage location through a simplified ray-tracing algorithm was detected.

5.1. Damage presence detection

Structural changes (e.g. cracks, plasticization and corrosion) appear in the TFR as either vertical lines or slanted lines (Chen and Ling, 2002) (Fig. 2). A similar behaviour is expected from perturbation waves reflected back by the structure boundaries. This explains why conventional UT needs skilled inspectors to discriminate the reflected waves due to structural changes from those due to structure boundaries. Therefore, at the aim to simplify the interpretation of the ultrasonic signals a brand new approach was developed. This was based on the idea that damage introduces, in the wave propagation phenomenon of the undamaged structure, an uncorrelated time signal due to the presence of waves reflected by the defect surface. Hence, in order to highlight the time discrepancy between the damaged and undamaged signal a coherence function based algorithm (CFBA) was used. The method was structured into two parts. The first involved the evaluation of a time–frequency coherence function, while the second phase identifies the presence of damages by discriminating between the time–frequency coherence changes due to noise and damage reflected wave arrivals.

In the first phase of the CFBA, the time–frequency coherence function, between the undamaged $s_u(t)$ and the damaged $s_d(t)$ signals, is evaluated as the ratio of the wavelet cross-spectrum S_{ud} and the product of the wavelet auto-spectra of the two time signals (S_{uu}, S_{dd}) (Kareem and Kijewski, 2002)

$$\text{CoH}(f,t) = \sqrt{\frac{|S_{ud}(f,t)|^2}{S_{uu}(f,t)S_{dd}(f,t)'}} \tag{5}$$

where the power spectra S_{uu}, S_{dd} and S_{ud} are given by

$$S_{ij}(f,t) = \int_0^t w_i^*(f,\tau)w_j(f,\tau)\mathrm{d}\tau \tag{6}$$

where i, j = {u,d}.

The integration time window $[0,t]$ in Eq. (6) was selected in the attempt to reduce the noise effects, which should be mitigated on a long time range. However, this process, together with noise, averages out, also, the changes in the coherence due to the arrival of the waves reflected by the damage surfaces. Therefore, a shorter time windows $[t-\Delta t, t+\Delta t]$ was also used to evaluate the power spectra
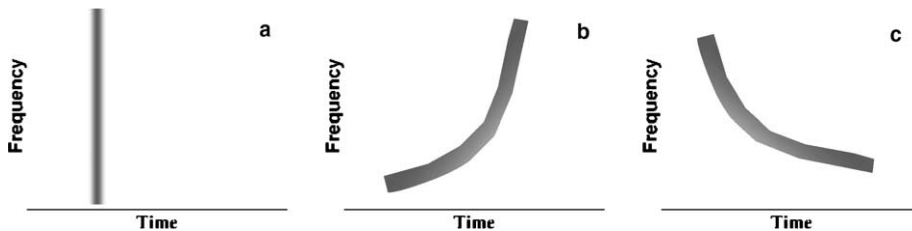

Fig. 2. Structural change scattering mechanisms: (a) surface discontinuity; (b) material dispersion; (c) waveguide structures.
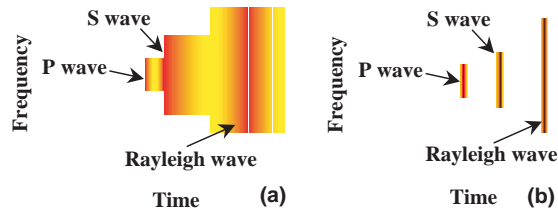
Fig. 3. Time–frequency coherence changes due to damage reflected waves.

$$S_{ij}(f, t) = \int_{t-\Delta t}^{t+\Delta t} w_i^*(f, \tau) w_j(f, \tau) \mathrm{d}\tau \qquad (7)$$

In both cases, the time discrepancies caused by noise appear as peaks randomly distributed in contrast with those due to defect reflected wave arrivals, which are characterised by sudden changes of the coherence along a wide frequency range. For the first time window chosen, the coherence change will extend in time and present rapid variation in coincidence of the arrivals of the wave reflected by the damage surface. In our case guided wave were used (see Fig. 3(a)). For the second time window considered $[t - \Delta t, t + \Delta t]$, the sudden coherence changes decrease shortly after to zero (see Fig. 3(b)).

Once, the damage presence is certain by recognising the behaviour described above, it is possible to proceed to the extraction of the echo start time as next section illustrates.

5.2. Echo start time extraction algorithm (ESTE)

The detection of the arrival times of the echoes is very important, because, the precision of the damage locations is strongly dependent on its correct estimation. At this extent, the echo start time extraction (ESTE) algorithm was developed. This consists in a two stage process. In the first stage, a pass-band noise filter reduces the noise effects and, then, the echo start time is identified by the evaluation of maxima lines. The pass-band noise filter effectiveness depends on two factors, the CWT tendency to concentrate the noise into high frequencies and the poor SNR at low frequencies due to the high frequency content of the signal discrepancy generated by the damage occurrence. In this way, two frequencies (f_1, f_2) are identified, which values rely on the SNR level respectively at low and high frequencies. At this point, the echo start time (echo arrival time) could be extracted by simply identifying, at each frequency, either the times at which the coherence has the most rapid change (for a time window $[0, t]$) or the time of coherence local maxima (for the later time window used). In both cases, the results will appear as a series of lines almost parallel to the frequency axis (Fig. 4, see black lines[1]). Unfortunately, the noise presence makes very difficult the extraction of the ridges and, in many cases, ends up in winding lines (red line in Fig. 4). Therefore, in order to minimise the noise effect on the time of flight extraction, the time frequency coherence was derived with respect to time. This highlights the wave arrivals as local maxima lines and reduces the winding behaviour showed in Fig. 4. Furthermore, a least square polynomial interpolation of the maxima lines identified can be used to improve the localisation of the wave arrivals.

Finally, the echo start time (t_{target}) is identified as function of the frequencies through the polynomial interpolation of the maxima lines of the time derivative of the time frequency coherence function relative to the first incoming S wave, Rayleigh and guided waves. Then, the localisation of the damage becomes possible as described in the next two sections.

---

[1] For interpretation of color in Fig. 4, the reader is referred to the web version of this article.
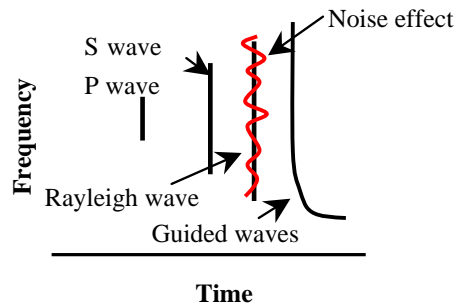
Fig. 4. Echo-start times.

5.3. Ray-tracing detection algorithm, theoretical background and set-up considerations

The wave propagation within solids is ruled by the Huygen's principle, the Fermat's principle and the Snell laws regulating the reflection and refraction phenomena (Graff, 1975). For the Huygen's principle (Graff, 1975) each point on a wavefront can be considered as a generation point for succeeding spherical waves. This means that, assuming the perturbation source so small to be reduced to a point, the wavefront generated are spherical with a radius equal to the product between the wave travelling speed (considered to be constant) and the travelling time. Moreover, for the principle of the least time (Fermat's), waves travel the fastest possible path between two points. Therefore, in uniform media, waves travel in space in straight lines. For media with boundaries, the wave propagation phenomenon is still governed by the same principles and laws, but for complex domain like rails, the travel path is not necessarily straight. In some cases, a further complication in the set-up of the defect localisation process is the impossibility to have the sensor location coincident with the excitation area as for the rails, where the excitation is provided by the train through the rail rolling surface. This means that a different location for the sensors must be chosen. For this selection, two factors must be taken into consideration. The first is related to the damage to be identified, for example, the rolling contact fatigue damages on rails. In other words, defects bounded on the railhead, which is a simple connected domain. The second factor is the sensitivity to structural changes of the sensor location, whose max value is located on the most flexible part of the rail, i.e. the web (Zumpano, 2005). In our research, the sensor was placed on the railhead but opposite to the rolling surface, since it was intended to be installed permanently on the rail in a position where the malfunctioning or destruction due to environmental loading and vandalism were minimized. This implies that the wave path is composed by two straight lines, the impinging line (from the excitation point up to the defect surface) and the reflected line ending in the sensor place (see Fig. 5).
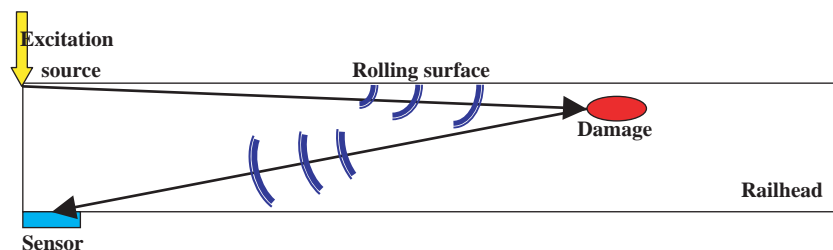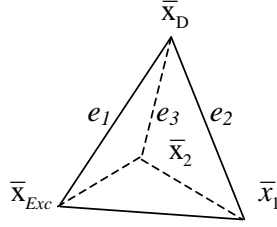

Fig. 5. Wave echo path.

Fig. 6. Tetrahedron of localisation.

The sensor number is determined by analysing the localisation problem from a mathematical point of view. Defining the domain $\Omega(x, y, z) \subset \Re^3$ (the structure) and $d\Omega(x, y, z)$ its surface, the probable damage position $\vec{x}_D$ is univocally identified by its three coordinates (unknowns). Therefore, three independent equations must be written in the three unknowns. In a 3D domains a point is univocally located as the vertex of a tetrahedron (Fig. 6), if and only if the locations of the other three vertices and the length of its edges are known.

Hence, considering a tetrahedron having as vertex $\vec{x}_D$, the excitation point $\vec{x}_{Exc}$ and two sensor locations $\vec{x}_1$, and $\vec{x}_2$, the edge lengths between $\vec{x}_{Exc}$, $\vec{x}_1$, $\vec{x}_2$ and $\vec{x}_D$ are unknown. The only known parameters are the wave path lengths from $\vec{x}_{Exc}$ to the two sensors ($\vec{x}_1$ and $\vec{x}_2$). Hence, only two independent equations can be identified Eq. (8), while for a well-posed problem three equations are needed.

$$
\begin{aligned}
e_1 + e_2 &= \ell_1 = t_{target1} c \\
e_1 + e_3 &= \ell_2 = t_{target2} c
\end{aligned}
\tag{8}
$$

where c is the speed of the waves (P, S, Rayleigh and guided waves) used to extract the t_{target}.

Each one of Eq. (8) defines the locus of the points (Weisstein, 2003) $\Gamma \subset \Re^3$ described by the vertex $\vec{x}_D$ of the triangle $\vec{x}_{Exc} \vec{x}_1 \vec{x}_D$ ($\vec{x}_{Exc} \vec{x}_2 \vec{x}_D$), whose distances e_1 and e_2 (e_3) from the two fixed points $\vec{x}_{Exc}$ and $\vec{x}_1$ (or, $\vec{x}_2$ the foci) give a constant sum equal to the wave path length ($\ell = \{\ell_1, \ell_2\}$) from to the first (second) sensor. Therefore, Γ is the surface of a revolution ellipsoid (Fig. 7) along the $\vec{x}_{Exc} \vec{x}_1$ ($\vec{x}_{Exc} \vec{x}_2$) direction. The ellipsoid equation in the canonical Cartesian coordinate system $X_c Y_c Z_c$, with the axis Y_c parallel to the direction of wave propagation Z and its origin (x_0, y_0, z_0) coincident with the mid point of the tetrahedron side $\vec{x}_{Exc} \vec{x}_1$ ($\vec{x}_{Exc} \vec{x}_2$), is
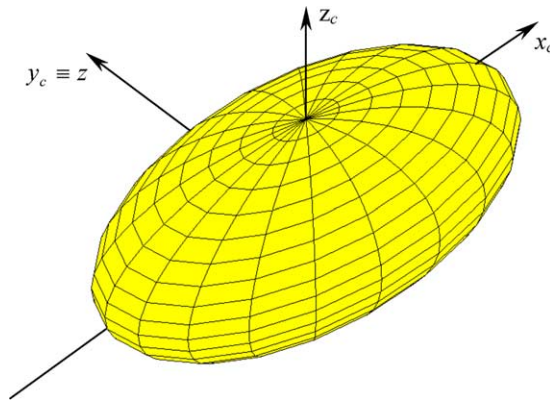

Fig. 7. Ellipsoid of the probable damage locations.

$$\frac{x_c^2}{a^2} + \frac{y_c^2}{b^2} + \frac{z_c^2}{c^2} = 1 \tag{9}$$

with the semi-axes lengths

$$a = \frac{\ell}{2}, \quad b = c = \frac{\ell}{2}\sin\theta, \quad \theta = a\cos\left(\frac{d(\vec{x}_{\mathrm{Exc}},\vec{x}_i)}{\ell}\right) \tag{10}$$

and $i = \{1,2\}$. The simultaneous satisfaction of Eq. (8) results in an ellipse, intersection of the two ellipsoids described by Eq. (9). This confirms that a third equation is needed. Two possible solutions were considered:

1. If a third point (sensor) $\vec{x}_3$ is selected and consequently a third ellipsoid is defined, the equation system, constituted by either the three ellipsoid Eq. (9) in the global coordinate system or equivalently in the form of Eq. (8), admits a unique solution if only if its Hessian is a positive definite matrix. Therefore, the locations of the sensors must be adjusted in order to fulfil this requirement for every $\vec{x}_D \in \Omega(x,y,z)$.
2. If damages are located only on the surface or next to it, the railhead surface equation can be used as the third independent equation

$$\mathrm{d}\Omega(x,y,z) = 0 \tag{11}$$

It is clear that the result of the geometric intersections, in most of the cases, yields two points. However, only one point will be in the direction of propagation. This point will identify the damage location. For structures that behave as waveguides (e.g. rails), an approximated solution can be obtained using only one sensor (one ellipsoid). This means that only the structure cross-section location of the damaged area, normal to the wave propagation direction, can be computed.

The single sensor approach is considered to be an appropriate solution for damage detection in waveguide structure. This reduces to the minimum the number of sensors and therefore the installation and the related maintenance expenses. The distance between two sensors deployed along the rail depends on the attenuation that the magnitude of the wave perturbations undergoes during the propagation phenomenon, the size of the minimum damage to identify, the range of frequencies investigated and the sensitivity of sensors and the acquisition devices. However, recent studies proved that some guided waves could propagate up to 2134 m (Rose et al., 2004). Based on these results sensors can be spaced every 300–600 m. However, the distance between two sets of sensors is still under investigation and will be the main topic of further publications.

5.4. Ray-tracing detection algorithm

The RTD algorithm locates the probable position of the damage by minimising the difference between the arrival times measured (t_{target}) and the numeric wave travel time (Fig. 5). For simplicity, in this section a single sensor was considered. However, the extension of the RDT algorithm to 2 or 3 sensors is straightforward. Since, the t_{target} is function of the frequency, either a single frequency or a range of frequencies can be used to evaluate the damage location. In the last case a least square optimisation algorithm is used. Here, for simplicity a single frequency was used. The main difference is that, in the case of a single frequency, t_{target} is a scalar instead of a vector (a coefficient for each frequency used) when a range of frequencies is used.

The wave travel time (12) is computed measuring, and summing up the Euclidean distances $d(\vec{x}_1,\vec{x}_2)$ between the probable damage position $\vec{x}_D$ and, respectively, the excitation location $\vec{x}_{\mathrm{Esc}}$ and the sensor position $\vec{x}_{\mathrm{Sens}}$, and then dividing for the wave speed c.

$$t(\vec{x}_\mathrm{D}) = \frac{d(\vec{x}_\mathrm{D}, \vec{x}_\mathrm{Exc}) + d(\vec{x}_\mathrm{D}, \vec{x}_\mathrm{Sens})}{c} \tag{12}$$

The minimisation of the wave travel time difference (WTTD, (13)) is carried out by an optimisation algorithm based on the quasi-Newton method (Coleman et al., 1999).

$$\mathrm{WTTD}(\vec{x}_\mathrm{D}) = |t_\mathrm{target} - t(\vec{x}_\mathrm{D})| \tag{13}$$

The optimisation process formulates, at each iteration, a quadratic model problem (14) through curvature information.

$$\min_{\vec{x}_\mathrm{D}} \frac{1}{2} \vec{x}_\mathrm{D}^\mathrm{T} H \vec{x}_\mathrm{D} + e^\mathrm{T} \vec{x}_\mathrm{D} + b \tag{14}$$

where H is the Hessian matrix of WTTD, e and b are respectively a constant vector and a constant. The optimal solution of the quadratic model problem occurs when its partial derivatives of $\vec{x}_\mathrm{D}$ tend to zero

$$\nabla \mathrm{WTTD}(\vec{x}_\mathrm{D}) = H\vec{x}_\mathrm{D} + e = 0 \tag{15}$$

Therefore, the optimal solution (the most probable damage position) was evaluated by

$$\vec{x}_\mathrm{D} = -H^{-1} e \tag{16}$$

The Hessian matrix evaluation in the quasi-Newton approach is performed by using the observed behaviour of WTTD and its gradient, in contrast with the pure Newton-type method, which calculates the Hessian matrix numerically involving a large amount of computation. In this case, the Hessian matrix is approximated by use of the BFGS formula (Coleman et al., 1999).

After the t_target was evaluated, the damage localisation with the developed damage detection algorithm was evaluated.

6. Validation of the wave propagation based damage detection algorithm

In order to test the wave propagation based damage detection (WPBDD) algorithm, numerical simulations of wave propagation phenomena on a rail sample, in pristine and damaged conditions, were carried out. In this paper, the effects of rolling contact fatigue damages, on the rail dynamic response, were considered. A FE model of the test case structure, using the commercial FE code ANSYS, was built. The test sample was 650 mm long (typical distance between two sleepers), whose foot was constrained at both its ends for 10 mm (half width of a sleeper). The damages introduced in the FE model were located on the railhead surface to simulate rolling contact fatigue defects (the most severe from the structure integrity point of view). Two single damages were considered.

6.1. Rail FE model

In this study, a particular rail was under investigation the 113A rail section (provided by Corus Group, see Fig. 8). The rail material stress–strain curve (Grade 220 rail steel) is shown in Fig. 9. The density was 7850 kg/m³ and the Poisson modulus was 0.33.

At the aim to capture correctly the wave propagation and avoid space aliasing, the mesh size was based on an approach (Bathe, 1982) used for finite difference analysis and method of characteristics that leads to an appropriate design of the mesh density and to the computation of the integration time step.

To describe with a sufficient resolution the phenomenon under investigation, it is necessary to define the size of the smallest characteristic of interest, termed critical wavelength (L_w). In the case studied, L_w was assumed equal to the size of the smallest damage to be detected along the wave propagation direction,
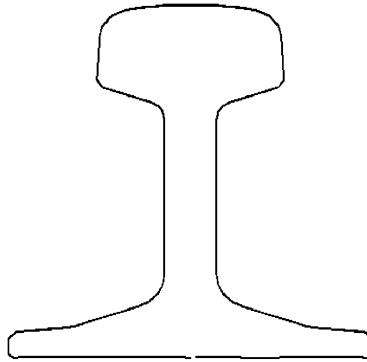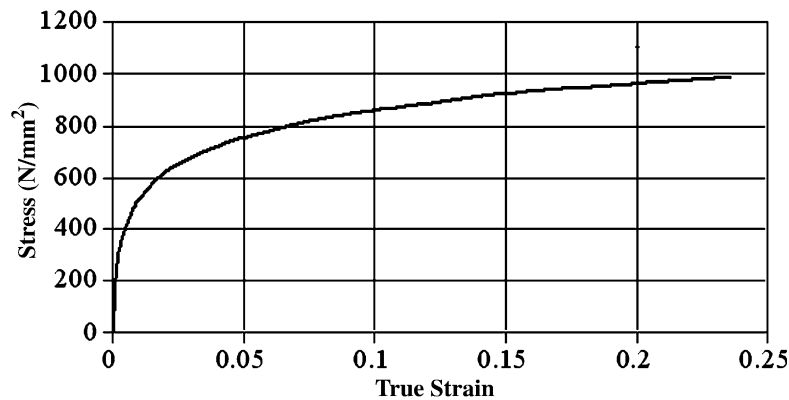
Fig. 8. Rail section 113A.

Fig. 9. Stress–strain curve for Grade 220 rail steel (Corus Group).

along the rail axis. As critical rolling contact fatigue damage, a defect 15 mm long, 5 mm large and 2 m deep was selected. According to the critical damage size, the transient analysis was carried out using a sampling time t_I (integration time) of 1.14 μs and finite element length (g) of 7.5 mm. The maximum frequency is related to the P wave speed, V_P (Cook et al., 1989; Bathe, 1982; Graff, 1975) and the FE length g (Eq. (17)). However, taking into account numerical errors and the approximation of Eq. (17) a safe factor (f_S) of 0.3 was considered.

$$f_{\max} = \frac{2V_P}{g}\frac{f_S}{2\pi} = \frac{2 \cdot 6560}{0.0075}\frac{0.3}{2\pi} \cong 83,500 \text{ Hz} \tag{17}$$

An impulsive excitation force was considered (a triangular step pulse lasting 1.14 μs) and applied on the railhead (Fig. 10). Two single site damaged scenarios (Fig. 10) were introduced at the middle and at 3/3 of the rail length from the excitation point. This type of damage was simulated by deleting two finite elements at the coordinates displayed in Tables 1 and 2. The damage size for both the damage cases was identical with a volume of 150 mm^3 and a weight of 1.2 g against a global weight of 36.6 kg of the rail portion investigated.

Only one sensor was used and placed opposed to both the rail-wheel contact surface and to the rail side where the damages were introduced (Fig. 10).
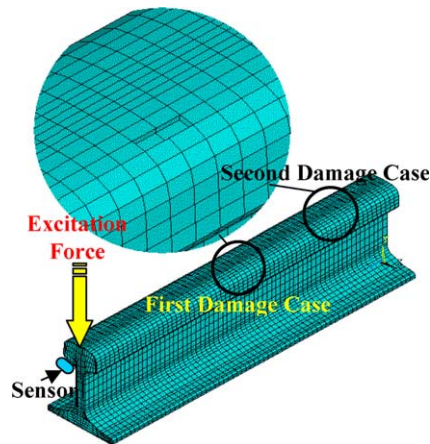
Fig. 10. Set-up configuration.

Table 1
First damaged scenario coordinates

| | Damage coordinates | | |
	X (mm)	Y (mm)	Z (mm)
Min	19.642	154.61	315.44
Max	25.117	157.58	330.56
Δ(max − min)	5.475	2.97	15.12

Table 2
Second damaged scenario coordinates

| | Damage coordinates | | |
	X (mm)	Y (mm)	Z (mm)
Min	19.642	154.61	150.94
Max	25.117	157.58	165.06
Δ(max − min)	5.475	2.97	15.12

The ANSYS transient solver, used for the analysis described above, was an implicit solver using the Newmark approach. To guarantee unconditioned convergence a structural damping was added through a logarithm decay parameter (0.05) (Konhke, 2001).

6.2. Results

The numerical data obtained by the FE analysis in form of displacements were converted into accelerations through a numeric derivation.

6.2.1. Analysis of the propagation phenomenon

The presence of structure boundaries alters the shape of the propagation wave fronts. However, according to Huygen's principle, their shapes tend to be spherical like as it can be observed in Fig. 11, where the displacements where pictured using a colour scale from blue to red according to their magnitude.
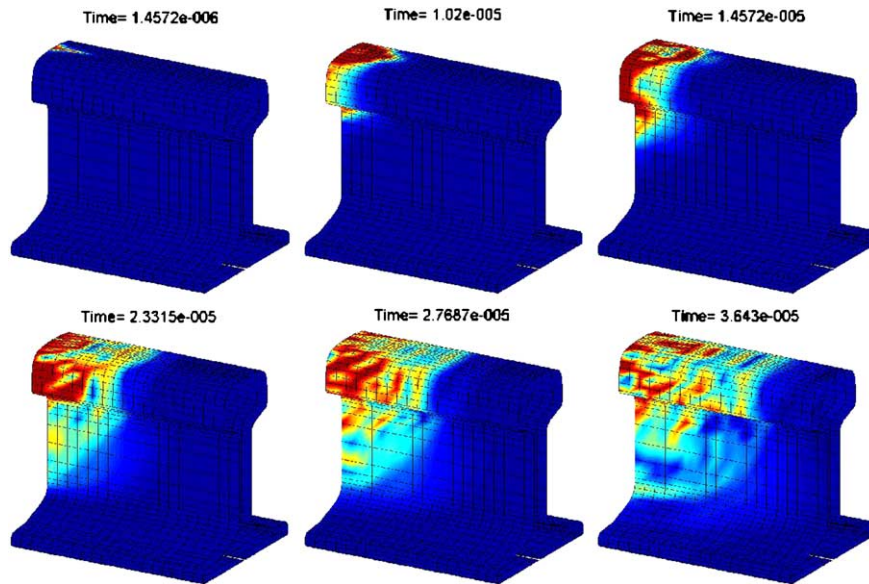
Fig. 11. Wave propagation due to impulsive excitation.

The damage presence introduces only visible changes in the rail dynamic response next to the damage location as pictured in Fig. 12(a) and (b). The damage occurrence can be highlighted by calculating the difference between the dynamic response of the damaged and the undamaged configuration as shown in Fig. 12(c). Using this approach the propagation of the perturbation introduced by the damage presence is magnified (Fig. 13). The perturbation propagation path is similar to that impulsive showed in Fig. 11. The intensity of discrepancy due to the damage introduction increases with the time because of the arrival

Fig. 12. Damage effect on wave propagation.

Fig. 13. Propagation of the perturbation introduced by the damage presence.

of guided waves with higher energy content. Moreover, the changes introduced by the damage presence propagate with larger magnitudes downstream the damage location rather than upstream (Fig. 13).

To detect the damage presence, the undamaged and damaged time histories in the time–frequency space were analysed. Because of the small damage introduced and the impulsive excitation provided, there are not

visible changes between time–frequency representations (TFRs) of the undamaged and damaged time signals (Fig. 14(a) and (b)). By analysing the difference between the damaged and undamaged TFR (Fig. 14(c)), the wave echoes due to the damage presence appear shifted with_respect to those showed in Fig. 14(a). A similar behaviour to that recorded in Fig. 14(b) is given by the time-frequency coherence (TFC) function of the undamaged and damaged time signals for both the time windows investigated ($[0, t], [t - \Delta t, t + \Delta t]$) as shown in Fig. 15.

Wave arrival times can be highlighted by evaluating the time derivative of the time–frequency coherence function. As shown in Fig. 16, the arrival of three high energy guided waves is very clear. A further proof of this is obtained by comparing the time derivative of the time–frequency coherence function and the time history of the damage perturbation, evaluated as the difference between the time histories of the damaged and the undamaged rail (Fig. 17, the coloured lines in this picture are the maxima lines identified). A first group of guided waves identified by the maxima line labelled 1, then, a second group with smaller amplitude referenced by the maxima line 2, were clearly identified (Fig. 17). Finally, a large group of waves is present (maxima lines from 3 to 8), but its shape does not resemble a unique group of waves, since the space
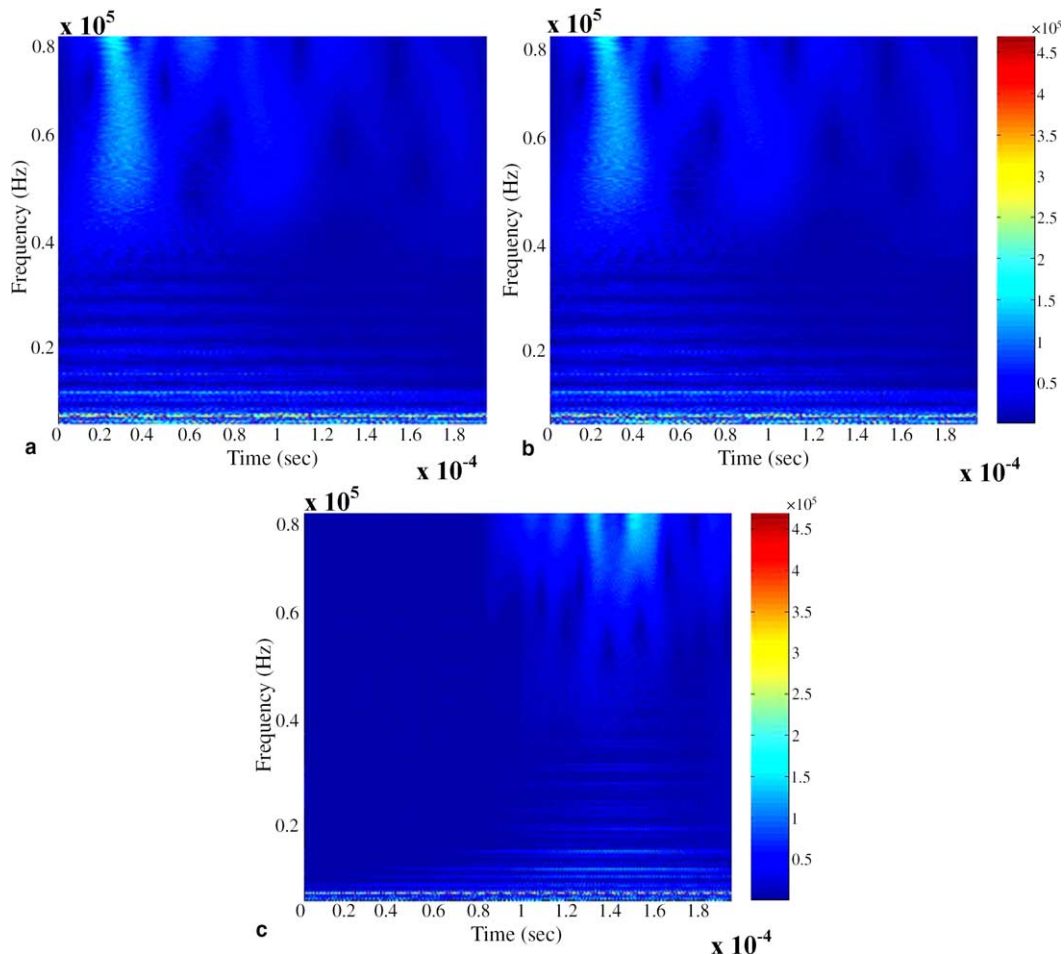

Fig. 14. TFR: (a) undamaged acceleration signal; (b) damaged acceleration signal (first damaged case); (c) differences between the CWTs of the damaged and the undamaged time signals.
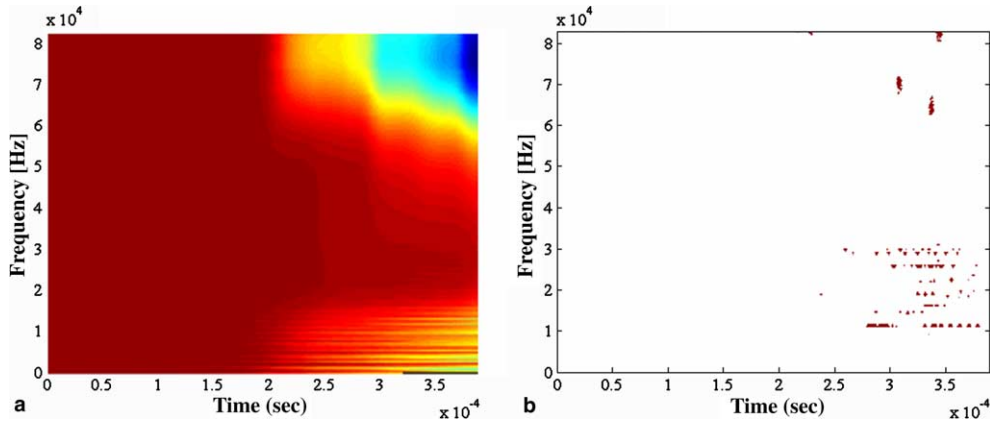
Fig. 15. Time frequency coherence (first single site damaged case): (a) $[0, t]$; (b) $[t - \Delta t, t + \Delta t]$.
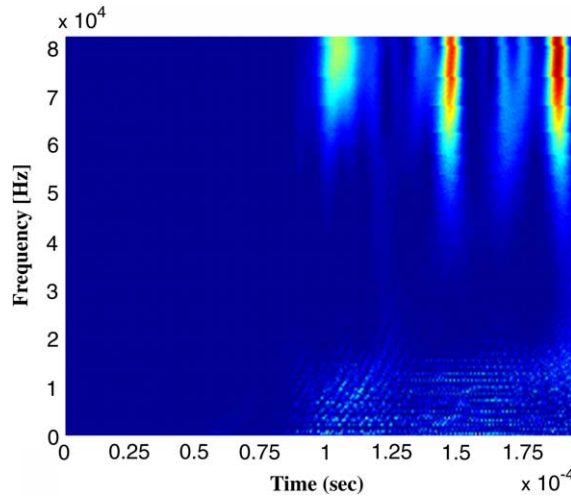

Fig. 16. Time derivative of the time–frequency coherence.

travelled was very short. Because of this uncertainty in the identification of the guided waves only the first wave group was used for the damage identification.

6.2.2. Guided wave velocity evaluation

The estimation of the guided wave velocities was carried out by modifying a joint time–frequency approach (Lanza di Scalea and McNamara, 2004). Instead of using the Gabor wavelet, a Morlet wavelet was adopted. The main difference, between the two, lays in the first term of the following equation (see Eq. (2)):

$$g(t) = \frac{1}{\sqrt[4]{\pi\gamma^2}} e^{-\frac{t^2}{\gamma^2}} (\cos(\omega_0 t) + i \sin(\omega_0 t)) \tag{18}$$

In order to satisfy a requirement for the Morlet wavelet ($\gamma\omega_0^2 \gg 1$), the two parameters, γ and f_0, were assumed equal to 0.25 and 10, for a $\gamma(2\pi f_0)^2 = 987$, well above 1.
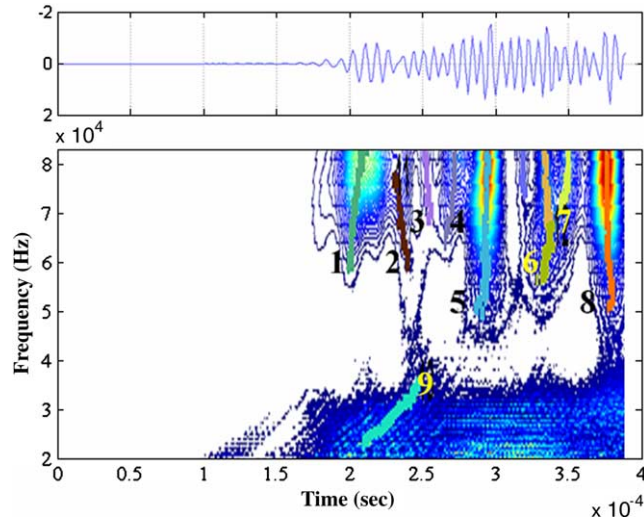
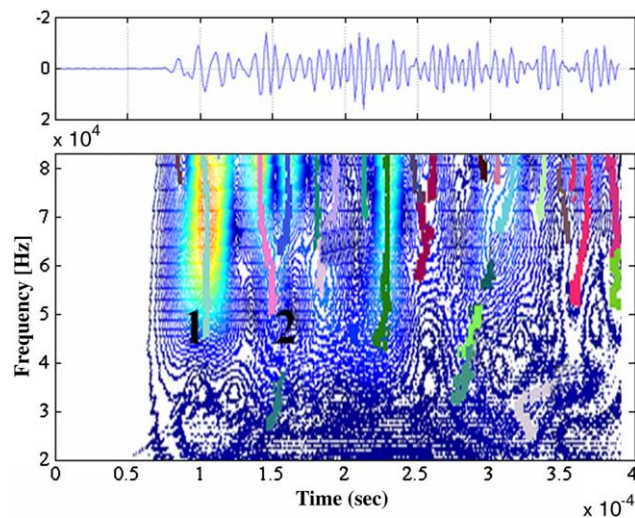Fig. 17. Maxima lines extraction from the time derivative of the time–frequency coherence.

Fig. 18. First section.

The guided wave velocities were estimated as the ratio of the distance between two sections (50 mm, the first section distant 325 mm from the excitation source and the second section located 50 mm from the fist in the wave propagation direction) and the time Δt needed to a selected guided wave to travel it. The time Δt was evaluated as the difference between the two maxima lines identifying the arrival times of the selected guided wave at the sections selected (Figs. 18 and 19).

By both the CWT representations showed above, it is clear that only the first guided wave is clearly identifiable. It was also possible to identify the shape of the wave propagation mode corresponding to the first maxima line of Figs. 18 and 19 (see Fig. 20). The shape of the propagation mode identified is clearly connected to the excitation source as suggested by the large compression region at the middle of the headrail top.
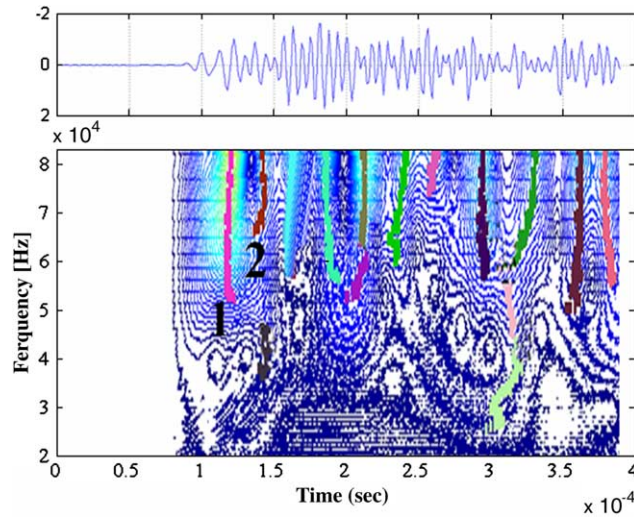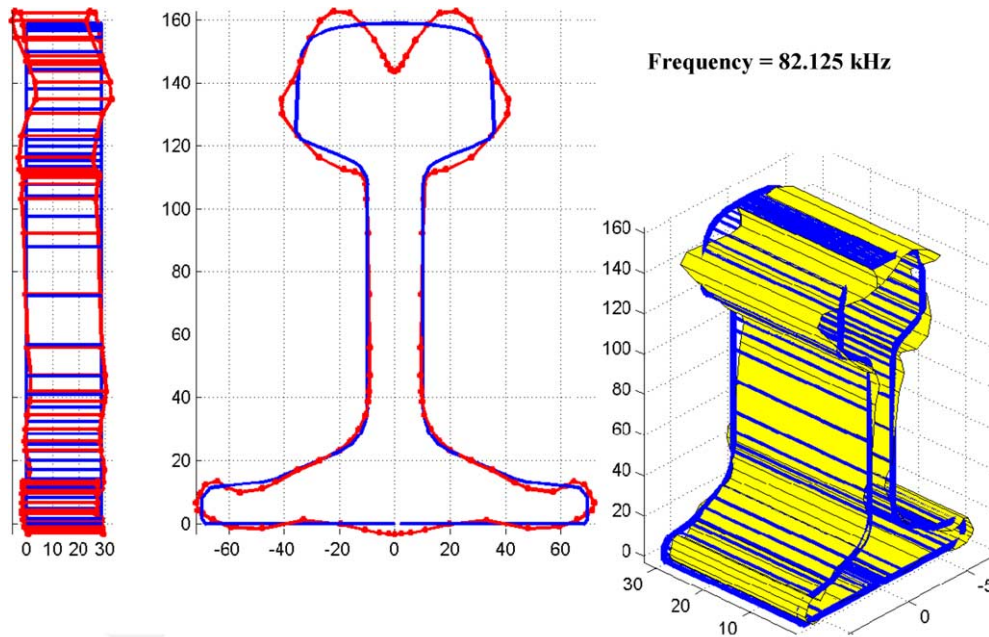
Fig. 19. Second section.

Fig. 20. Shape of the wave propagation mode identified by the maxima line 1 at 82.125 kHz.

The speed of the guided wave was plotted against the frequency in Fig. 21.

The guided wave showed a non-dispersive behaviour with the increase of the frequency as for the guided wave showed in (Lanza di Scalea and McNamara, 2004). Unfortunately, a direct comparison with the values found in literature (Lanza di Scalea and McNamara, 2004) could not be made, since the maximum frequency at which the guided wave velocity evaluated in literature (8000 Hz) is well below the minimum

frequency investigated in this paper. In Fig. 21, although the top frequency is well above the maximum meaningful frequency (83.5 kHz) evaluated in Eq. (17), the guided wave velocity behaviour resembles the physical conduct of experimental and numerically derived guided wave velocities (Cawley et al., 2002; Lanza di Scalea and McNamara, 2004).

6.2.3. Damage identification

Because the acquisition system configuration was constituted by only one sensor, only the damaged cross-section was identified. For the first damage scenario investigated, the first guided wave was identified by the maxima line labelled 1 (Fig. 17). Therefore, using the maxima line 1 time points as t_{target}, the damage location was detected as a function of the frequency as shown in Fig. 22.
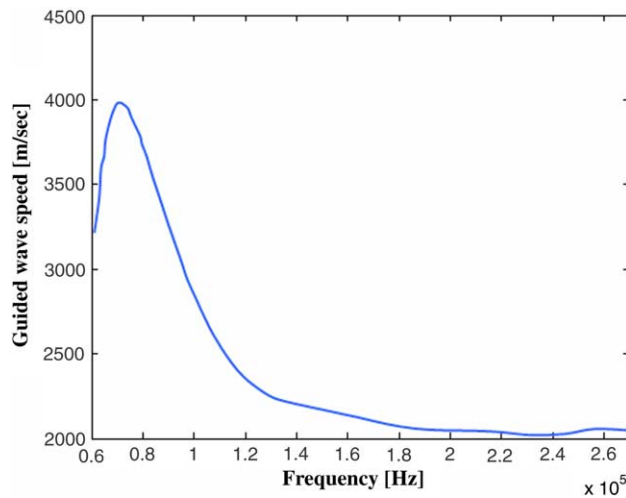

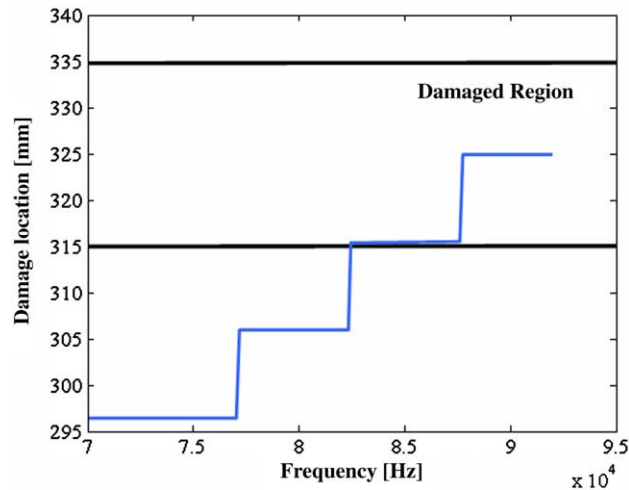Fig. 21. Guided wave velocity extracted.

Fig. 22. First damage scenario.

The damage was precisely localised for a range of frequency that goes from 82 to 92 kHz. In contrast, for smaller frequency the damage was localised with a variable error smaller than 20 mm. The main reason for such behaviour is caused by the different spatial resolutions of the damage detection algorithm presented. This is related to the wavelength of the impinging wave on the damage surface, this goes from about 60 mm at 70 kHz to 40 mm at 90 kHz. Therefore, the damage localisation below 82 kHz are in accordance with those given at higher frequencies. The damage location in Fig. 22 varies in steps because a discrete optimisation algorithm, able to identify as damage location only nodes of the rail FE model, was used.

In the second damaged scenario investigated, the discrepancy introduced by damage presence has, in the time derivative of the time–frequency coherence function for the first guided wave (Fig. 23), a shorter frequency range and smaller amplitude compared to that introduced by the first damage scenario investigated (Fig. 17). Such amplitude and frequency loss is related to the attenuation phenomenon due to the natural damping of the material. The reduced amplitude of the local maxima might be the reason for an erroneous selection of the guided wave maxima line, since at high frequencies, the maxima can become comparable to numerical errors generated by the FE code and by the numerical derivations carried out to convert displacements into accelerations.

This concern is confirmed by the behaviour of the identification of the damage location with the frequency showed in Fig. 24. The error in the identification of the damage location increases with the frequency, although it is in any case smaller than the spatial resolution (smaller than 40 mm), evaluated before.

The damage localisation above presented is independent from the magnitude of the excitation used. This comes particular handy, when the excitation is provided by a coming or an already passed train. It is clear that in such event, the nature of the excitation is slightly different from the point shape here simulated and, therefore, so the type of the wave propagation mode excited will be different. Consequently, also the guided wave generated by the train transit will be different.

The authors are aware of the fact that an extensive numerical and experimental campaign focused on the identification and the recording of the guided wave properties and behaviour, with more typologies of damages, is needed. However, the positive results presented show that the approach is promising and a good margin of improvement can be achieved on longer samples, where the guided wave with larger energy contents are sufficiently separated from each other.

The separation and the characterisation of single modes will be crucial for the identification of different types of rail defects. The damage severity can be also assessed by relating the magnitude of the changes of the time frequency coherence to the reflection and the attenuation coefficients of each guided wave used.
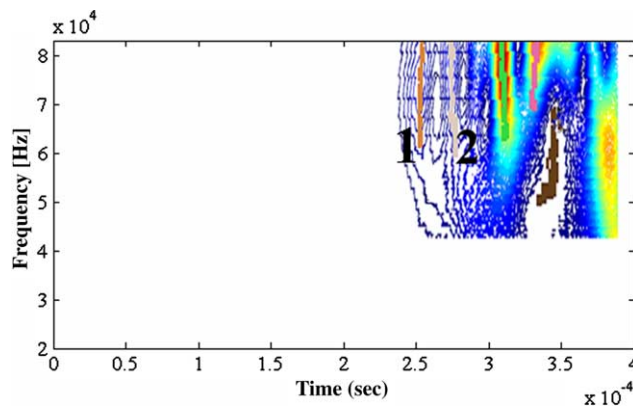

Fig. 23. Time derivative of the time–frequency coherence function for the second damage investigated.
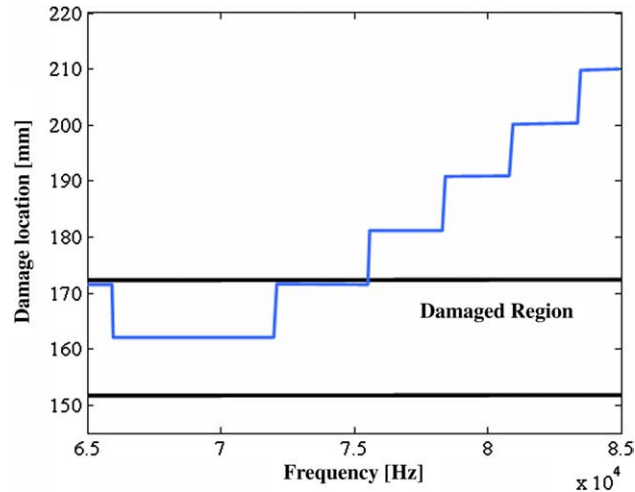
Fig. 24. Second damage scenario localisation.

Another important aspect is that the proposed methodology can be quasi real-time, since the runtime is of the order of tens of seconds, and with the increase of computer power it is envisaged that it can become near time in a non-distant future.

Further studies should be carried out on the selection of the best range of frequency to use, according to the type of damage to be identified. These investigations will be dominated by two main contrasting factors, the spatial resolution and the attenuation phenomenon. Both increase with the frequency. Consequently, if high spatial resolutions are required, shorter portion of rail can be scanned and more sensors will be necessary. Therefore, it is clear that a compromise between these two opposite driving requirements must be found.

7. Conclusion

This paper presents a wave based fault detection technique aimed at detecting and localising structural surface damage on rail structures. The proposed method is based on the idea that the damage introduces, in the wave propagation an uncorrelated time signal due to the presence of waves reflected by the defect surface. The uncorrelations are generated by waves reflected back to the sensor locations by the flaw surfaces. The damage is localised by identifying the discrepancies, due to damage presence, between the undamaged and the damaged time signals in the wave propagation phenomenon analysed (*P*, *S*, Rayleigh and guided waves).

The damage detection methodology developed was split in three steps. In the first step, the presence of the damage on the structure was assessed. The time discrepancy between the damaged and undamaged signal was calculated by using a coherence function based algorithm (CFBA). In the second step, the arrival time of the reflected wave (or echo) was estimated using the continuous wavelet transform. Then, the detection algorithm was able, through a ray-tracing algorithm, to estimate the location of damage.

Numerical investigations of two single damages were carried out. The damage was introduced on the railhead surface to simulate rolling contact fatigue defects. The results showed that the proposed methodology can successfully localise the damage location, however, as expected, the localisation is strongly affected by the frequency range used. The results also showed that the separation and the characterisation

of single modes will be crucial for the identification of different types of rail defects. Further work is needed to establish damage severity by relating the magnitude of the changes of the time frequency coherence to the reflection and the attenuation coefficients of each guided wave used and on the selection of the best range of frequency according to the type of damage to be identified.

References

Abbaszadeh, K., Rahimian, M., Toliyat, H.A., Olson, L.E., 2003. Rails defect diagnosis using wavelet packet decomposition. IEEE Transactions on Industry Applications 39 (5).

Angrisani, L., Daponte, P., 1997. Thin thickness measurements by means of a wavelets transform-based method. Measurement 20 (4), 227–242.

Bathe, K.-J., 1982. Finite Element Procedures in Engineering Analysis. Prentice-Hall Inc., Englewood Cliffs, NJ.

Bohmer, A., Klimpel, T., 2002. Plastic deformation of corrugated rails—a numerical approach using material data of rail steel. Wear 253, 150–161.

Bruzelius, K., Mba, D., 2004. An initial investigation on the potential applicability of Acoustic Emission to rail track fault detection. NDT&E International 37 (7), 507–516.

Cannon, D.F., Pradier, H., 1996. Rail rolling contact fatigue research by the European Rail Research Institute. Wear 191, 1–13.

Cannon, D.F., Edel, K.-O., Grassie, S.L., Sawley, K., 2003. Rail defects: an overview. Fatigue and Fracture of Engineering Materials and Structures 26, 865–887.

Cawley, P., Lowe, M.J.S., Alleyne, D.N., Pavlakovic, B., Wilcox, P., 2002. Practical long range guided wave testing: applications for pipes and rail. Material Evaluation—American Society for Nondestructive Testing 61 (1), 66–74.

Chen, V.C., Ling, H., 2002. Time-Frequency Transformation for Radar Imaging and Signal Analysis. Artech House, Boston, London.

Clark, R., 2004. Rail flaw detection: overview and need for future developments. NDT&E International 37, 111–118.

Coleman, T., Branch, M.A., Grace, A., 1999. Optimisation Toolbox. User's Guide, Version 2, The Math Works Inc.

Cook, R.D., Malkus, D.S., Plesha, M.E., 1989. Concepts and Applications of Finite Element Analysis, third Ed. John Wiley & Sons, Chichester, UK.

Eadie, D.T., Kalousek, J., Chiddick, K.C., 2000. The role of high positive friction (HPF) modifier in the control of short pitch corrugation and related phenomena. In: Contact Mechanics 2000 Conference, Tokyo. Available from: <http://www.kelsan.com/007_publications.html>.

Franklin, R., Halabe, U.B., Gopalakrishnan, B., 2001. NDT Solution-Knowledge based assistant for ultrasonic testing methodology of materials. American Society for Nondestructive Testing. Available from: <http://www.asnt.org/publications/materialseval/solution/dec01solution/dec01sol.htm>.

Gilliam, X., Dunyak, J., Doggett, A., Smith, D., 2000. Coherent structure detection using wavelet analysis in long time-series. Journal of Wind Engineering and Industrial Aerodynamics 88, 183–195.

Graff, K.F., 1975. Wave Motion in Elastic Solids. Clarendon Press, Oxford.

Grassie, S., Nilsson, P., Bjurstrom, K., Frick, A., Hansson, L.G., 2002. Alleviation of rolling contact fatigue on Sweden's heavy haul railway. Wear 253, 42–53.

Hay, T.R., Rose, J.L., 2002. Guided wave testing optimization. Material Evaluation—American Society for Nondestructive Testing 60 (10), 1239–1252.

Jeffrey, B.D., Peterson, M.L., 1999, Assessment of rail flaw inspection data. Mountain–Plains Consortium, Report No. MPC-99-106. Available from: <http://www.ndsu.nodak.edu/ndsu/ugpti/MPC_Pubs/pdf/MPC99-106.pdf>.

Jeong, D.Y., 2001. Progress in rail integrity research. Federal Railroad Administration, Department of Transportation, Report DOT/FRA/ORD-01/18.

Kareem, A., Kijewski, T., 2002. Time–frequency analysis of wind effects on structures. Journal of Wind Engineering and Industrial Aerodynamics 90, 1435–1452.

Kenderian, S., Djordjevic, B.B., Green Jr., R.E., 2001. Point and line source laser generation of ultrasound for inspection of internal and surface flaws in rail and structural materials. Research in Nondestructive Evaluation 13, 189–200.

Konhke, P., 2001. ANSYS Inc. Theory Manual, twelfth ed., SAS IP Inc.

Lanza di Scalea, F., McNamara, J., 2003. Ultrasonic NDE of railroad tracks: air-coupled cross-sectional inspection and long-range inspection. Insight 45 (6), 394–401.

Lanza di Scalea, F., McNamara, J., 2004. Measuring high-frequency wave propagation in railroad tracks by joint time–frequency analysis. Journal of Sound and Vibration 273 (3), 637–651.

Legendre, S., Goyette, J., Massicotte, D., 2001. Ultrasonic NDE of composite material structures using wavelets coefficients. NDT&E International 34 (1), 31–37.

Lundgren, J.R., Cannon, D.F., Zuber, P., 2001. An international cooperative research approach for rail defect risk management. In: 7th International Heavy Haul Association Conference, Brisbane, Australia.

Mallat, S., 1998. A Wavelet Tour of Signal Processing. Academic Press., London.

Mandelis, A., Munidasa, M., Nicolaides, L., 1999. Laser infrared photothermal radiometric depth profilometry of steel and its potential in rail track evaluation. NDT&E International 32, 437–443.

Mandriota, C., Stella, E., Nitti, M., Ancona, N., Distante, A., 2001. Rail corrugation detection by Gabor filtering. In: International Conference on Image Processing, IEEE, vol. 2. pp. 626–628.

Marais, J.J., Mistry, K.C., 2003. Rail integrity management by means of ultrasonic testing. Fatigue and Fracture of Engineering Materials and Structures 26, 931–938.

Markov, A.A., Shpagin, D.A., Shilov, M.N., 2003. Ultrasonic multichannel flaw detector for testing rails with signal recording. Russian Journal of Nondestructive Testing 39 (2), 105–114.

Mueller, S., 2000. A linear wheel-rail model to investigate stability and corrugation on straight track. Wear 243, 122–132.

Murav'ev, V.V., Boyarkin, E.V., 2003. Nondestructive testing of the structural-mechanical state of currently produced rails on the basis of the ultrasonic wave velocity. Russian Journal of Nondestructive Testing 39 (3), 24–33.

Oukhellou, L., Aknin, P., Perrin, J.-P., 1999. Dedicated sensor and classifier of rail head defects. Control Engineering Practice 7, 57–61.

Rose, J.L., 2000. Elastic wave analysis for broken rail detection. In: 15th WCNDT, Rome. Available from: <http://www.ndt.net/article/wcndt00/papers/idn270/idn270.htm>.

Rose, J.L., Avioli, M.J., Mudge, P., Sanderson, R., 2004. Guided wave inspection potential of defects in rail. NDT&E International 37, 153–161.

Staszwski, W.J., 1997. Identification of damping in MDOF systems using time-scale decomposition. Journal of Sound and Vibration 203 (2), 283–305.

Takacs, N., Posgay, G.Y., Harasztosi, L., Beke, D.L., 2002. Correlation between Barkhausen-noise and corrugation of railway rails. Journal of Material Science 37, 3599–3601.

Teolis, A., 1998. Computational Signal Processing with Wavelets. Birkhauser, Boston.

Vadillo, E.G., Tarrago, J.A., Zubiaurre, G.G., Duque, C.A., 1998. Effect of sleeper distance on rail corrugation. Wear 217, 140–146.

Viktorov, I.A., 1967. Rayleigh and Lamb Waves: Physical Theory and Application. Plenum Press, New York.

Weisstein, E.W., 2003. Ellipse, Wolfram Research Inc. www.mathworld.wolfram.com/Ellipse.html.

Wilcox, P., Evans, M., Pavlokovic, B., Alleyne, D., Vine, K., Cawley, P., Lowe, M., 2003. Guided wave testing of rail. Insight 45 (6), 413–420.

Zumpano, G., 2005. Damage detection on mechanical and aeronautical structures. Ph.D. Thesis, Cranfield University.